Open Archive TOULOUSE Archive Ouverte (OATAO)
OATAO is an open access repository that collects the work of Toulouse researchers and makes it freely available over the web where possible.

This is an author-deposited version published in : http://oatao.univ-toulouse.fr/
Eprints ID : 16021

To link to this article : DOI:10.1103/PhysRevLett.117.074502
URL : http://dx.doi.org/10.1103/PhysRevLett.117.074502

To cite this version : Zami-Pierre, Frédéric and de Loubens, Romain and Quintard, Michel and Davit, Yohan *Transition in the Flow of Power-Law Fluids through Isotropic Porous Media.* (2016) Physical Review Letters, vol. 117. 074502/1-074502/5. ISSN 0031-9007

Any correspondence concerning this service should be sent to the repository administrator: staff-oatao@listes-diff.inp-toulouse.fr

Transition in the Flow of Power-Law Fluids through Isotropic Porous Media

F. Zami-Pierre,[1,2] R. de Loubens,[2] M. Quintard,[1] and Y. Davit[1,*]
[1]*Institut de Mécanique des Fluides de Toulouse (IMFT)–Université de Toulouse, CNRS-INPT-UPS, Toulouse France*
[2]*Total, CSTJF, Avenue Larribau, 64018 Pau, France*

We use computational fluid dynamics to explore the creeping flow of power-law fluids through isotropic porous media. We find that the flow pattern is primarily controlled by the geometry of the porous structure rather than by the nonlinear effects in the rheology of the fluid. We further highlight a macroscale transition between a Newtonian and a non-Newtonian regime, which is the signature of a coupling between the viscosity of the fluid and the structure of the porous medium. These complex features of the flow can be condensed into an effective length scale, which defines both the non-Newtonian transition and the Newtonian permeability.

DOI: 10.1103/PhysRevLett.117.074502

The creeping flow of complex fluids through porous media embraces a wide variety of applications such as blood flow in vascular networks [1] or enhanced oil recovery [2–4]. Understanding and modeling such systems has proven a considerable challenge, as they intricately couple the nonlinear effects of non-Newtonian fluids with the multiscale nature of porous media. Linear transport phenomena in porous materials can often be described using homogenized equations encapsulating the large deviations induced by the multiscale heterogeneities—one of the hallmarks of transport in porous media—in a limited number of effective parameters. When the large deviations induced by the porous structure are further coupled with the rich nonlinear behaviors displayed by the flow of complex fluids—shear thickening and thinning, yield and cutoff effects, time-dependent mechanisms, confinement and sorption effects—it becomes unclear whether or not such average descriptions can accurately describe momentum transport. For a shear-thinning fluid, a strong nonlinear response could yield preferential flow paths whereby the fluid might primarily flow at large velocity in regions where it would exhibit a relatively small viscosity, while leaving almost at rest other regions where it exhibits a higher viscosity (see similar effects in computations for Bingham fluids in Ref. [5]).

One would expect that such nonlinear mechanisms would make Darcy's law obsolete. In many instances, however, surprisingly simple generalizations of Darcy's law have been shown to adequately describe the flow of non-Newtonian fluids in porous media. For pure power-law fluids, a modified version where $\langle U\rangle^n \propto \|\nabla\langle P\rangle_{\mathrm{FL}}\|$, with $\langle U\rangle$ the velocity norm [6], $\langle P\rangle_{\mathrm{FL}}$ the hydrodynamic pressure, and n a power-law coefficient, has been validated experimentally [7–10], computationally [11–13], and theoretically [14–19]. When the fluids further display yield or cutoff effects, there are also examples of simple macroscopic laws describing the flow. For instance, Chevalier and co-workers in Refs. [9,10] show that, even though channels may develop in a transition regime, a generalized Darcy law can be used for Bingham fluids with the yield stress described as a critical pressure gradient at the macroscale. A similar approach is used for the flow of polymer solutions behaving as power-law fluids with cutoff (PLCO), i.e., displaying a Newtonian regime below a critical value of the shear rate $\dot{\gamma}_c$. At the macroscale, these are often modeled using Newtonian and non-Newtonian regimes with a transition characterized empirically by a set of parameters, an equivalent shear rate, and an effective length scale based on the square root of the Newtonian permeability [20–25].

These studies suggest that the porous medium may not systematically amplify nonlinear effects and induce large perturbations in the flow pattern. Recent studies in Refs. [10,13], combining experimental measurements of the flow with theoretical analyses and computations on model systems, suggest that the primary mechanism controlling the flow pattern is the geometrical constriction of the flow, which dominates nonlinear effects. These studies also demonstrate that there is a significant lack of understanding in the fundamental physics of non-Newtonian flow through porous media, particularly concerning the link between the microscale physics and the apparent macroscale behavior. In this Letter, we use computational fluid dynamics to study (1) nonlinear effects in the rheology of PLCO fluids and their attenuation in the porous medium, (2) the validity of Darcy's law, and (3) the transition from a Newtonian to a non-Newtonian regime.

To this end, we explore numerically the flow of PLCO fluids in a broad variety of porous geometries including complex realistic structures obtained using x-ray microtomography. We use the following generalized steady-state Stokes equation to describe the flow:

$$\nabla\cdot\left[\mu(\dot{\gamma})\left(\nabla\mathbf{U}+(\nabla\mathbf{U})^{\mathsf{T}}\right)\right]-\nabla P=0, \qquad (1)$$

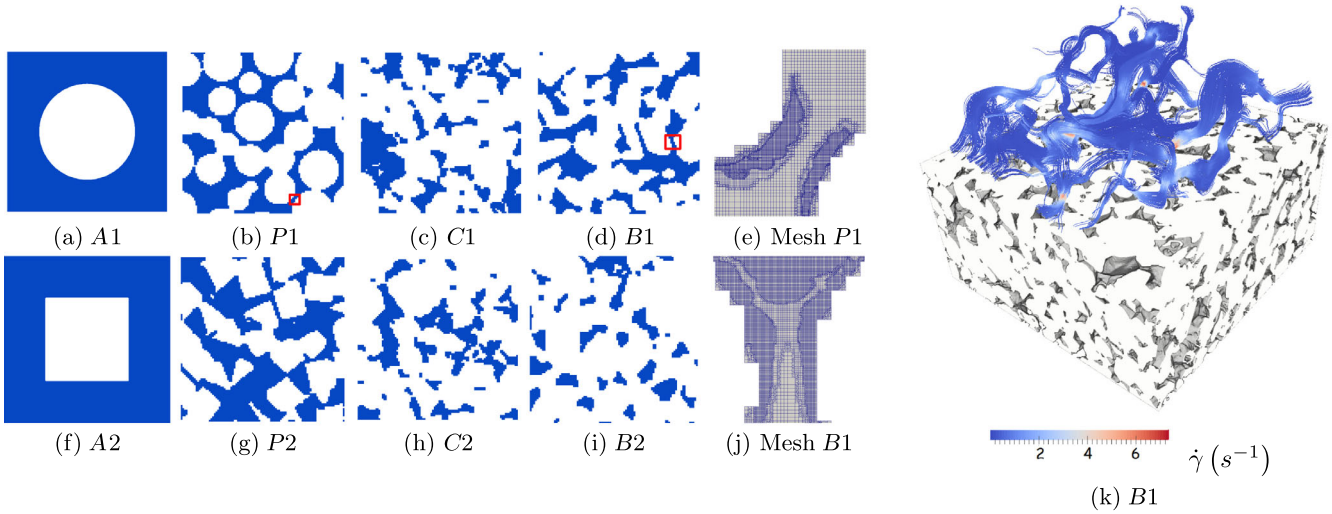

FIG. 1. Geometries of the porous structures. (a)–(d), (f)–(i) Two-dimensional slices of the porous media investigated. $A1$ and $A2$ are two-dimensional arrays of cylinders and squares. $P1$ and $P2$ are three-dimensional packings of beads and cuboids. $C1$ and $C2$ are subvolumes of a Clashach sandstone sample. $B1$ and $B2$ are subvolumes of a Bentheimer sandstone sample. Media P, C, and B were obtained using x-ray microtomography. (e),(j) Illustration of the mesh used for the flow calculation in the pore throats. (k) Three-dimensional representation of the porous medium with the geometry of $B1$ in the lower half and the corresponding streamlines colored by shear rate in the upper half, illustrating the strong localization of viscous dissipation.

where $\mathbf{U}$ is the velocity field, which further satisfies $\nabla \cdot \mathbf{U} = 0$, and P is the pressure field. The viscosity is a power law with a simple cutoff in the limit of low shear rates:

$$\mu(\dot{\gamma}) = \begin{cases} \mu_0 & \text{if } \dot{\gamma} < \dot{\gamma}_c \\ \mu_0 \left(\frac{\dot{\gamma}}{\dot{\gamma}_c}\right)^{n-1} & \text{otherwise,} \end{cases} \tag{2}$$

where μ_0 is the viscosity in the Newtonian limit, $\dot{\gamma} = \sqrt{\frac{1}{2}(\nabla\mathbf{U} + (\nabla\mathbf{U})^{\mathsf{T}}) : (\nabla\mathbf{U} + (\nabla\mathbf{U})^{\mathsf{T}})}$, and $\dot{\gamma}_c$ is the cut-off value of the shear rate above which non-Newtonian effects occur. The parameter n characterizes the response of the fluid to the shear rate with $n < 1$ corresponding to shear thinning and $n > 1$ to shear thickening. This expression of the viscosity is known to properly describe the flow of a number of polymer solutions such as xanthan or dextran [7,8,26] and the two parameters n and $\dot{\gamma}_c$ can be measured via standard rheological methods. For convenience, we further define the following averaging operators, $\langle \bullet \rangle_{\mathrm{FL}} = (1/|\Omega_{\mathrm{FL}}|) \int_{\Omega_{\mathrm{FL}}} \bullet dV$, $\langle \bullet \rangle = (1/|\Omega|) \int_{\Omega_{\mathrm{FL}}} \bullet dV$, where Ω_{FL} is the fluid domain and Ω the whole domain (including the solid phase). These operators are simply connected via the relation $\langle \bullet \rangle = \phi_{\mathrm{FL}} \langle \bullet \rangle_{\mathrm{FL}}$, with $\phi_{\mathrm{FL}} = |\Omega_{\mathrm{FL}}|/|\Omega|$ the volume fraction of the fluid domain.

The Stokes equation is solved using the finite-volume toolbox OpenFOAM [27] via a SIMPLE algorithm [28] with second-order discretization in space. We use boundary conditions similar to permeameters, whereby a macroscale pressure gradient is obtained by imposing a uniform pressure on the inlet and outlet faces and no-slip conditions on other faces. A no-slip condition is also used at the liquid-solid interface, therefore not accounting for slip effects observed with polymer solutions [29]. For each medium, an unstructured polyhedral mesh (hex dominant) was generated and convergence was carefully studied. To achieve grid convergence while maintaining the number of elements tractable, we performed local refinements within the pore throats; see Figs. 1(j) and 1(e). For each three-dimensional structure, we used approximately 10^8 mesh cells, and the entire work required about 10^5 cores $\times$ h on the supercomputer EOS-CALMIP.

Eight porous media (see Fig. 1) are investigated, six of which are three-dimensional (1 mm^3)—two Bentheimer sandstones, $B1$ and $B2$; two Clashach sandstones, $C1$ and $C2$; and 3D packings of beads $P1$ and cuboids $P2$—and the other two are two-dimensional (1 mm^2) arrays of cylinders $A1$ and squares $A2$. The three-dimensional structures were all obtained using x-ray computed microtomography, along with standard reconstruction, filtering, and segmentation techniques [30–32]. We do not detail these here, as x-ray tomography data were merely used as a way to generate complex digital structures exhibiting realistic geometrical and topological features.

We characterize each structure using the porosity ϕ_{FL}, in the range 0.1–0.7, along with the length scales ℓ_{min}, ℓ_{max}, and $\ell_{\mathrm{corr}(\chi)}$, which were calculated from chord lengths distributions and spatial autocorrelation of the fluid indicator function χ (see Refs. [33,34]) on samples of identical sizes. The arrays $A1$ and $A2$ are ordered (largest correlation length $\ell_{\mathrm{corr}(\chi)}$) with the lowest ratio $\ell_{\mathrm{max}}/\ell_{\mathrm{min}}$. The packings $P1$ and $P2$ are moderately disordered (intermediate correlation length) with slightly larger differences between

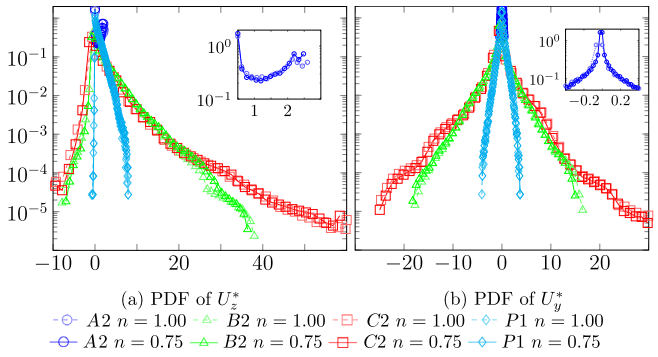

FIG. 2. PDFs of the dimensionless longitudinal $U_z^* = U_z/\langle U\rangle$ and transverse $U_y^* = U_y/\langle U\rangle$ components of the velocity fields for four porous media under Newtonian ($n = 1.00$) and non-Newtonian ($n = 0.75$ and more than 80% of the fluid being non-Newtonian) flow conditions. Insets correspond to a magnification of the PDFs for $A2$. Lines are a guide to the eyes.

the largest and smallest pores. The sandstones B and C are highly disordered (smallest correlation length) and display a broad distribution of pore sizes with the largest ratio $\ell_{\max}/\ell_{\min}$. Further details are given in the Table 1 of the Supplemental Material [35].

Our calculations in the Newtonian regime exhibit some of the statistical properties typical of porous media, as can be measured experimentally (see, e.g., Refs. [38]). The flow is not completely random, but rather is correlated with a structure that depends on the pore scale geometry (see Fig. 1 in Ref. [35]). The structure of the correlation function is similar for the packings and arrays with a decay over a length scale that is about the object's size. For the sandstones B and C, however, we find a length scale that is smaller, suggesting a larger amount of randomness in the velocity fields.

The probability density functions (PDFs) of the velocity fields, Fig. 2, are markedly different between the porous media. The PDFs of the two-dimensional arrays are distinctly the narrowest, displaying only cocurrent flow and relatively small variations in velocity in comparison with three-dimensional media. For all three-dimensional structures, the cocurrent component of the longitudinal velocity exhibits first a near exponential decay, but with a much steeper slope for the packings (see also Refs. [38–40] for media similar to $P1$). The sandstones are characterized by a broader range of countercurrent flow and a distribution of the largest velocities that deviates from an exponential decay, a result that may have important implications for mass dispersion models [39,40]. Consistent with Ref. [38], we also find that the distributions of transverse velocities for all media are not Gaussian, but are roughly symmetric (isotropy) with near exponential decay.

The PDFs of the normalized velocity fields (Fig. 2) and the correlation functions (Fig. 1 in Ref. [35]) are nearly invariant with respect to the flow regime, highlighting that the statistics for non-Newtonian flow are only slightly perturbed from the Newtonian case. This is in sharp

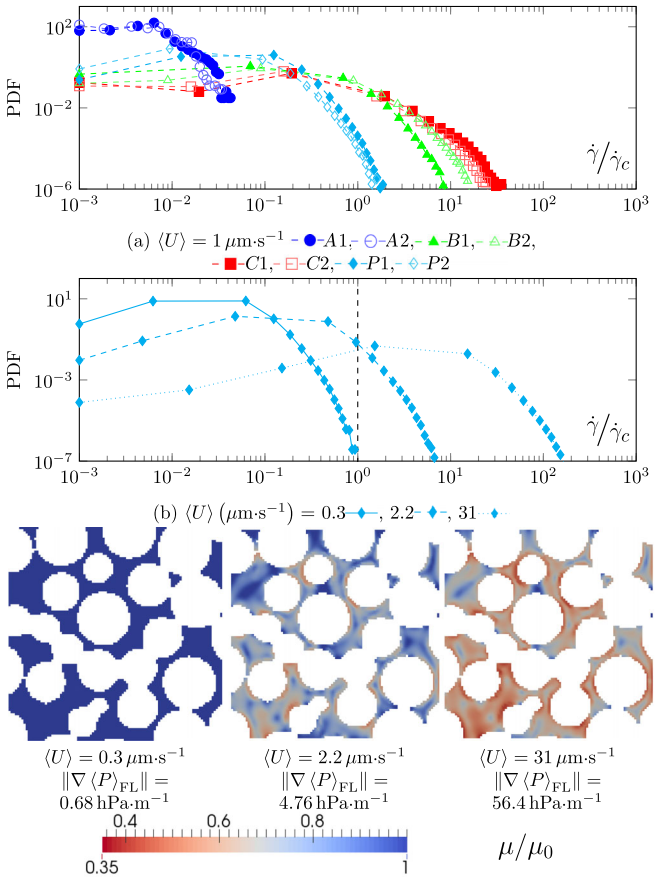

(c) Dimensionless viscosity field, μ/μ_0, for medium $P1$.

FIG. 3. PDFs of the shear rate for (a) an average velocity 1 $\mu\text{m}\cdot\text{s}^{-1}$ for all eight media and (b) medium $P1$ at different flow regimes. (c) Normalized viscosity field for $P1$ and the three average velocities in (b). Rheology: $\dot\gamma_c = 1\ \text{s}^{-1}$ and $n = 0.75$. Lines are a guide to the eyes.

contrast with the large above-described differences in the flow statistics between porous structures [see also PDFs for shear rates in Fig. 3(a)], suggesting that the flow pattern is controlled by the porous structure which dominates nonlinear effects. This type of negative feedback between the porous medium and the nonlinear rheology was already observed for Bingham fluids in Refs. [10,13,41].

For each medium, we study the flow as the pressure gradient, and therefore the average velocity, is increased [see PDFs of the shear rate for $P1$ in Fig. 3(b)]. In the limit of small pressure gradients, the maximum value of the shear rate remains below $\dot\gamma_c$. As the average velocity increases, the distributions of the shear rate progressively translate towards larger values of $\dot\gamma$ until the pore throats and regions close to surfaces where the shear rate is maximum reach $\dot\gamma_c$ and become non-Newtonian. As we further increase the pressure gradient, the domain that is affected progressively extends towards the centers of the pores [see Fig. 3(c) and Ref. [35]). Eventually, for large average velocities, the whole fluid domain becomes

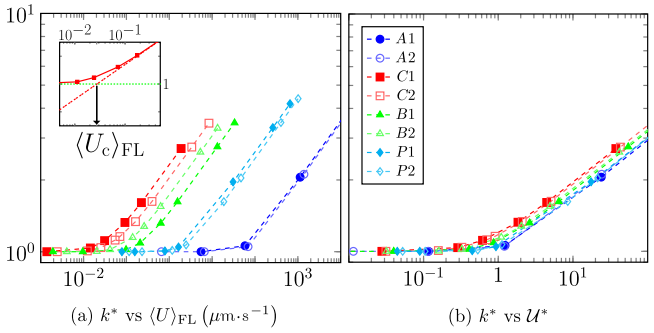

(a) k^* vs $\langle U \rangle_{FL}$ $(\mu m \cdot s^{-1})$ (b) k^* vs $\mathcal{U}^*$

FIG. 4. Apparent dimensionless permeability $k^* = k/k_0$ against (a) the average velocity $\langle U \rangle_{FL}$ and (b) the dimensionless velocity $\mathcal{U}^* = \langle U \rangle_{FL}/(\dot{\gamma}_c \sqrt{k_0})$. The inset is a magnification of the transition for $C1$, showing precisely how $\langle U_c \rangle_{FL}$ is calculated. Rheology: $\dot{\gamma}_c = 1 s^{-1}$ and $n = 0.75$. Lines are a guide to the eyes.

non-Newtonian. The transition for the different porous structures is similar, the primary difference being the value of $\langle U \rangle_{FL}$ at which the fluid starts to exhibit a non-Newtonian behavior, which is correlated with the geometrical properties of the medium (see Ref. [35]).

We now focus on the macroscale behavior of PLCO fluids and consider the validity of Darcy's law, $\langle \mathbf{U} \rangle = -\mu_0^{-1} k \nabla \langle P \rangle_{FL}$. We study an apparent dimensionless permeability $k^* = k/k_0$, where k_0 is the Newtonian permeability, which is determined numerically by calculating the velocity $\langle \mathbf{U} \rangle$ corresponding to an imposed pressure gradient $\nabla \langle P \rangle_{FL}$. Results in Fig. 4(a) show two different regimes for all porous media. In the limit of small average velocity, the fluid is Newtonian and can be described via Darcy's law with a constant permeability. In the limit of large average velocity, the shear rate exceeds the critical value for every point in the fluid and we obtain a modified Darcy's law with $\langle U \rangle^n \propto \|\nabla \langle P \rangle_{FL}\|$. Between these two limits, we observe a relatively short transition joining smoothly Darcy's law to the regime $\langle U \rangle^n \propto \|\nabla \langle P \rangle_{FL}\|$. The transition can be further characterized by a critical velocity $\langle U_c \rangle_{FL}$ defined as in Fig. 4(a). This critical velocity is the signature of a multiscale effect where the cutoff in the rheology of the bulk fluid combines with the structure of the porous medium to yield a transition characterized by the average velocity.

Interestingly, the macroscale non-Newtonian regime is attained before every fluid point has become non-Newtonian at the microscale. We therefore hypothesize that the macroscale transition corresponds to the change in the rheology of only a subdomain of Ω_{FL}, Ω_{PT}, that controls the flow. Once Ω_{PT} is non-Newtonian, the macroscale behavior rapidly becomes fully non-Newtonian, with $\langle U \rangle^n \propto \|\nabla \langle P \rangle_{FL}\|$, even though the microscale rheology remains a complex mixture of Newtonian and non-Newtonian fluids [as illustrated in Figs. 3(b) and 3(c) herein and in Fig. 2 in Ref. [35]]. This phenomenon can be further explored to develop an analytical expression of $\langle U_c \rangle_{FL}$ in terms of k_0, using the idea that Ω_{PT} also controls the global viscous dissipation (a detailed derivation is given in Ref. [35]). A dimensional analysis for the critical velocity first yields $\langle U_c \rangle_{FL} = \dot{\gamma}_c \ell_{eff}$, where ℓ_{eff} is an effective length scale that can be estimated as $\ell_{eff} = \ell_{PT}/\beta$ using a characteristic pore throat length ℓ_{PT}, an acceleration parameter $\beta = (\langle U \rangle_{PT}/\langle U \rangle_{FL}) > 1$ and a pore-throat averaging operator defined as $\langle \bullet \rangle_{PT} = (1/|\Omega_{PT}|) \int_{\Omega_{PT}} \bullet dV$. Using energetic considerations, we express the permeability in terms of the global viscous dissipation as

$$k_0 = \frac{\mu_0 \langle U \rangle^2}{\langle \mathcal{E} \rangle}, \tag{3}$$

where $\mathcal{E}$ is the local rate of dissipated energy by viscous forces per unit volume. Assuming that $\mathcal{E}$ is strongly localized in Ω_{PT} (see Ref. [35]), we finally obtain

$$\ell_{eff} \simeq \sqrt{k_0}. \tag{4}$$

Figure 4(b) confirms this theory numerically, showing that the dimensionless velocity $\mathcal{U}^* = \langle U \rangle_{FL}/(\dot{\gamma}_c \sqrt{k_0})$ predicts the transition with relatively good accuracy, without any fitting parameter.

In this Letter, we used computational fluid dynamics to study nonlinear effects in the flow of PLCO fluids through isotropic homogeneous porous media—the impact of anisotropies and heterogeneities being an important extension of this work. Our first result is that the nonlinear effects only weakly impact the flow statistics (PDFs, correlation lengths) and that the primary mechanism controlling the flow pattern is the geometrical constriction of the flow, not the non-Newtonian rheology. Secondly, we find that a relatively small subdomain Ω_{PT}, not the whole fluid, determines the transition to a macroscopic non-Newtonian regime where $\langle U \rangle^n \propto \|\nabla \langle P \rangle_{FL}\|$. The third result of this Letter is a theory providing an analytical formulation for the critical velocity at which we obtain macroscale transition. This theory uses the idea that Ω_{PT} controls both the viscous dissipation and the non-Newtonian transition to show that the effective length scale, $\ell_{eff} \simeq \sqrt{k_0}$, accurately approximates the transition velocity. Interestingly, we remark that $\sqrt{k_0}$ is already used to characterize other nonlinear effects in porous media, such as the transition from a linear (Darcy) to a quadratic drag (Darcy-Forchheimer) [42]. This study substantiates the role of the length scale $\sqrt{k_0}$ in porous media sciences and suggests a certain degree of universality in the mechanisms governing nonlinear flows through porous media.

We thank Total for the support of this study. This work was granted access to the HPC resources of CALMIP supercomputing center under the allocation 2015-11.

*yohan.davit@imft.fr

[1] J. V. Soulis, G. D. Giannoglou, Y. S. Chatzizisis, K. V. Seralidou, G. E. Parcharidis, and G. E. Louridas, Medical Engineering and Physics **30**, 9 (2008).

[2] E. Koval, Soc. Pet. Eng. J. **3**, 145 (1963).
[3] L. W. Lake, R. Johns, W. Rossen, and G. Pope, *Fundamentals of Enhanced Oil Recovery* (Society of Petroleum Engineers, Richardson, 1986).
[4] K. S. Sorbie, *Polymer-Improved Oil Recovery* (Springer Science and Business Media, 2013).
[5] T. Chevalier and L. Talon, Phys. Rev. E **91**, 023011 (2015).
[6] The notation $\langle U \rangle$ corresponds to $\|\langle \mathbf{U} \rangle\|$, not to $\langle \|\mathbf{U}\| \rangle$.
[7] G. Chauveteau and N. Kohler, Soc. Petrol. Eng. J. **24**, 361 (1984).
[8] R. S. Seright, T. Fan, K. Wavrik, and R. d. C. Balaban, Soc. Petrol. Eng. J. **16**, 35 (2011).
[9] T. Chevalier, C. Chevalier, X. Clain, J. Dupla, J. Canou, S. Rodts, and P. Coussot, J. Non-Newtonian Fluid Mech. **195**, 57 (2013).
[10] T. Chevalier, S. Rodts, X. Chateau, C. Chevalier, and P. Coussot, Phys. Rev. E **89**, 023002 (2014).
[11] A. F. Morais, H. Seybold, H. J. Herrmann, and J. S. Andrade, Jr., Phys. Rev. Lett. **103**, 194502 (2009).
[12] M. Vakilha and M. T. Manzari, Transport Porous Med. **74**, 331 (2008).
[13] J. Bleyer and P. Coussot, Phys. Rev. E **89**, 063018 (2014).
[14] O. Gipouloux and A.-M. Zine, Comput. Geosci. **1**, 127 (1997).
[15] S. Liu and J. H. Masliyah, Chem. Eng. Sci. **53**, 1175 (1998).
[16] D. Getachew, W. Minkowycz, and D. Poulikakosi, J. Porous Media **1**, 273 (1998).
[17] J.-L. Auriault, P. Royer, and C. Geindreau, Int. J. Eng. Sci. **40**, 1151 (2002).
[18] Z. Idris, L. Orgéas, C. Geindreau, J.-F. Bloch, and J.-L. Auriault, Model. Simul. Mater. Sci. Eng. **12**, 995 (2004).
[19] X.-H. Wang, J.-T. Jia, Z.-F. Liu, and L.-D. Jin, J. Porous Media **17**, 741 (2014).
[20] K. Sorbie and Y. Huang, J. Colloid Interface Sci. **145**, 74 (1991).
[21] A. Fletcher, S. Flew, S. Lamb, T. Lund, E. Bjornestad, A. Stavland, N. Gjovikli *et al.*, in *Proceedings of the SPE International Symposium on Oilfield Chemistry* (Society of Petroleum Engineers, 1991).
[22] G. Chauveteau, J. Rheol. **26**, 111 (1982).
[23] J. Lecourtier and G. Chauveteau, Macromolecules **17**, 1340 (1984).
[24] P. Zitha, G. Chauveteau, and A. Zaitoun, in *Proceedings of the SPE International Symposium on Oilfield Chemistry* (Society of Petroleum Engineers, San Antonio, 1995).
[25] M. Delshad, G. A. Pope, and K. Sepehrnoori, Center for Petroleum and Geosystems Engineering, The University of Texas at Austin, Texas 78751, 21 (2000).
[26] V. B. Veljkovic, M. L. Lazić, and D. U. Skala, Enzyme Microb. Tech. **10**, 686 (1988).
[27] H. G. Weller, G. Tabor, H. Jasak, and C. Fureby, Comput. Phys. **12**, 620 (1998).
[28] S. V. Patankar, in *Numerical Heat Transfer and Fluid Flow*, Series in Computational Methods in Mechanics and Thermal Sciences (Hemisphere Publishing Corporation, New York, 1980).
[29] F. Brochard and P. De Gennes, Langmuir **8**, 3033 (1992).
[30] H. Andrä, N. Combaret, J. Dvorkin, E. Glatt, J. Han, M. Kabel, Y. Keehm, F. Krzikalla, M. Lee, C. Madonna, M. Marsh, T. Mukerji, E. H. Saenger, R. Sain, N. Saxena, S. Ricker, A. Wiegmann, and X. Zhan, Comput. Geosci. **50**, 25 (2013).
[31] M. Piller, D. Casagrande, G. Schena, and M. Santini, J. Phys Conf. Ser. **501**, 012010 (2014).
[32] O. Rozenbaum and S. R. du Roscoat, Phys. Rev. E **89**, 053304 (2014).
[33] A. Jongerius, D. Schoonderbeek, A. Jager, and S. Kowalinski, Geoderma **7**, 177 (1972).
[34] M. Ioannidis, M. Kwiecien, and I. Chatzis, J. Petrol. Sci. Eng. **16**, 251 (1996).
[35] See Supplemental Material at http://link.aps.org/supplemental/10.1103/PhysRevLett.117.074502 for additional details about the porous structures, the representation in terms of probability density functions, the flow statistics, the transition mechanism and the corresponding theory, which includes Ref. [36,37].
[36] I. Cousin, P. Levitz, and A. Bruand, Eur. J. Soil Sci. **47**, 439 (1996).
[37] M. Pilotti, S. Succi, and G. Menduni, Europhys. Lett. **60**, 72 (2002).
[38] S. S. Datta, H. Chiang, T. S. Ramakrishnan, and D. A. Weitz, Phys. Rev. Lett. **111**, 064501 (2013).
[39] Y. Kutsovsky, L. Scriven, H. Davis, and B. Hammer, Phys. Fluids **8**, 863 (1996).
[40] R. S. Maier, D. Kroll, Y. Kutsovsky, H. Davis, and R. S. Bernard, Phys. Fluids **10**, 60 (1998).
[41] B. D. Rabideau, P. Moucheront, F. Bertrand, S. Rodts, N. Roussel, C. Lanos, and P. Coussot, J. Non-Newtonian Fluid Mech. **165**, 394 (2010).
[42] J. Lage and B. Antohe, J. Fluids Eng. **122**, 619 (2000).

Supplemental Material: Transition in the Flow of Power-Law Fluids through Isotropic Porous Media

F. Zami-Pierre[1,2], R. de Loubens[2], M. Quintard[1] and Y. Davit[1]*
[1] *Institut de Mécanique des Fluides de Toulouse (IMFT) - Université de Toulouse, CNRS-INPT-UPS, Toulouse France and*
[2] *Total, CSTJF, Avenue Larribau, 64018 Pau, France*

This document contains supplementary materials to our paper *Transition in the Flow of Power-Law Fluids through Isotropic Porous Media*. We provide additional details about the porous structures, the representation in terms of probability density functions, the flow statistics, the transition mechanism and the corresponding theory.

I. POROUS MEDIA STATISTICS

The eight porous media investigated in this study exhibit very different geometrical structures, as characterized in Table I. In addition to the porosity ϕ_{FL}, we analyze the geometry of each porous medium using several standard metrics. A chord distribution is calculated according to the method of Jongerius [1] with $\ell_{\min}$ defined as the first peak in the distribution [2] and $\ell_{\max}$ the longest chord. Auto-correlation functions (see [3, 4]) are also calculated for the fluid indicator function χ, which value is 1 in the liquid phase and 0 in the solid phase, and the velocity fields, $\mathbf{U}$. The characteristic length scale $\ell_{\mathrm{corr}(\chi)}$, defined as the integral of the auto-correlation function, is specific to the spatial structure [4], while $\ell_{\mathrm{corr}(\mathbf{U})}$ characterizes the velocity fields. Table I also contains the values of the Newtonian permeability, k_0, for each medium and the critial velocity at which the macroscale transition occurs (calculated for $\dot{\gamma}_c = 1\,\mathrm{s}^{-1}$).

Medium	$A1$	$A2$	$P1$	$P2$	$B1$	$B2$	$C1$	$C2$
$\ell_{\min}$	400	500	22	20	11	12	10	9
$\ell_{\max}/\ell_{\min}$	2.5	2	4.2	4.5	5.4	5.3	6.2	6.3
$\ell_{\mathrm{corr}(\chi)}$	150.4	159.4	32.6	53.8	26.5	27.2	29.8	29.3
$\ell_{\mathrm{corr}(\mathbf{U})}$	210	222	104	55.8	34.5	35.1	32.5	33.2
$\sqrt{k_0}$	105	115	5.76	6.63	1.39	0.91	0.53	0.70
k_0	11005	13121	33.2	44	1.92	0.82	0.27	0.48
$\langle U_c \rangle_{\mathrm{FL}}$	88.7	92.8	5.88	6.15	1.21	0.633	0.272	0.387
ϕ_{FL}	0.72	0.75	0.38	0.44	0.18	0.17	0.13	0.14
ϕ_{PT}	0.175	0.252	0.085	0.10	0.025	0.022	0.010	0.014
$\phi_{\mathrm{FL}}/\sqrt{\phi_{\mathrm{PT}}}$	1.72	1.49	1.20	1.39	1.13	1.20	1.30	1.18

TABLE I Characteristic properties of the eight porous media (lengths in μm, k_0 in μm^2, $\langle U_c \rangle_{\mathrm{FL}}$ in $\mu m.s^{-1}$), illustrating the variety of the porous structures. $\ell_{\min}$, $\ell_{\max}$ and ℓ_{corr} are characteristic lengths. ϕ_{FL} and ϕ_{PT} are the volume fractions of, respectively, the fluid domain and the pore throats. k_0 is the Newtonian permeability. $\langle U_c \rangle_{\mathrm{FL}}$ is the critical velocity for the non-Newtonian transition.

II. PROBABILITY DENSITY FUNCTIONS

In our study, the three-dimensional velocity and shear rate fields are presented using probability density functions (PDFs). These are obtained directly from the discrete representation of the finite-volume calculations. For a field f, we construct the PDF, $p(f)$, as follows. We first calculate the minimum and maximum values of the field f, $\min(f)$ and $\max(f)$, and discretize f in a finite number of intervals between $\min(f)$ and $\max(f)$. For each point in the PDF, $p\left(f_i\right)$ is obtained by calculating the volume of the mesh elements for which $f_{i-1} \leq f < f_i$, with the first point of the PDF, $p\left(f_1\right)$, describing $\min(f) \leq f < f_1$. Finally, these values are normalized as $p^*\left(f_i\right) = \frac{p(f_i)}{\sum_i p(f_i)\delta f_i}$, with $\delta f_i = f_i - f_{i-1}$, so that the area under the PDF equals one, $\sum_i p^*\left(f_i\right)\delta f_i = 1$.

III. CORRELATION FUNCTIONS

We calculate the correlation function, $C_{\mathbf{UU}}$, of the velocity deviation $\delta\mathbf{U} = \mathbf{U} - \langle \mathbf{U} \rangle_{\mathrm{FL}}$, with $\langle \bullet \rangle_{\mathrm{FL}} = \frac{1}{|\Omega_{\mathrm{FL}}|}\int_{\Omega_{\mathrm{FL}}} \bullet dV$, as (see also [5])

$$C_{\mathbf{UU}}(\|\mathbf{h}\|) = \left\{ \frac{\sum_j \delta\mathbf{U}\left(\mathbf{r}_j\right) \cdot \delta\mathbf{U}\left(\mathbf{r}_j + \mathbf{h}\right)}{\sum_j \delta\mathbf{U}\left(\mathbf{r}_j\right) \cdot \delta\mathbf{U}\left(\mathbf{r}_j\right)} \right\}. \qquad (1)$$

The brackets $\{\bullet\}$ represent an average over all xyz directions (calculated numerically using 6 points at $+/-\|\mathbf{h}\|$ in each direction) and the summation over the index j corresponds to all cell points of an associated Cartesian grid obtained by linear interpolation. For comparison with experimental results in [5], we also calculated $C_{\mathbf{UU}}$ for two-dimensional planes xz through $P1$.

The correlation functions, which provide a metric for disorder [4], are presented in Fig. 1 and values of $\ell_{\mathrm{corr}(\mathbf{U})}$ are summarized in Table I. We observe sharp exponential decays, especially for B and C, characterized by a short length scale $\ell_{\mathrm{corr}(\mathbf{U})}$. For $P1$, the two-dimensional correlation decays similarly to the three-dimensional one, but with much stronger fluctuations on a length scale about the diameter of the beads. The comparison between Newtonian and non-Newtonian curves further highlights the weak impact of the nonlinearity on the flow pattern.

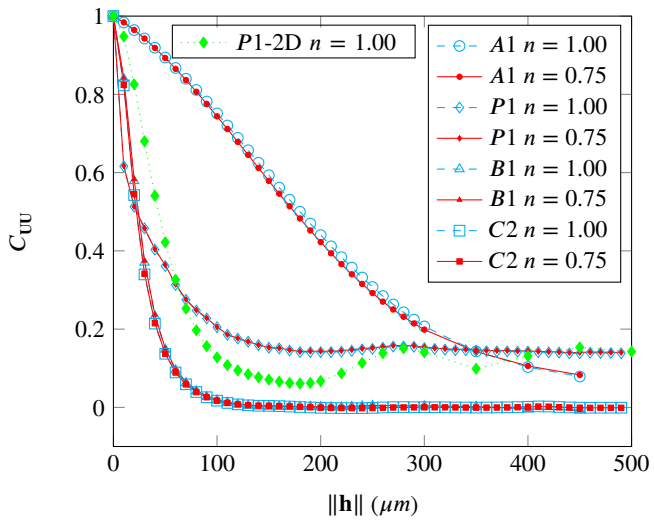

FIG. 1 Plots of the correlation functions $C_{\mathbf{UU}}$ as functions of the distance $\|\mathbf{h}\|$ for the different classes of porous media in the Newtonian and non-Newtonian regimes. Lines are a guide to the eyes.

IV. EVOLUTION OF THE VISCOSITY WITH THE PRESSURE GRADIENT

In this Section, we provide supplementary material to the Fig. 3 in the main article by presenting data for additional porous structures. Fig. 2 shows dimensionless representations of the viscosity fields for array $A2$, packing $P2$ and the sandstones $B2$ and $C2$. The first column corresponds to a value of the average velocity that is below the critical value for the non-Newtonian transition ($\mathcal{U}^* < 1$). We see that the viscosity field is uniform, which corresponds to a Newtonian situation. The center column corresponds to the critical value of the average velocity ($\mathcal{U}^* = \mathcal{O}(1)$) and shows that only a small subdomain of the fluid has transitioned to a non-Newtonian behavior with $\mu \neq \mu_0$. The initial transition occurs primarily in the pore throats for B and C. For P and A, we observe a larger subdomain also including the vicinity of the pore walls. The third column corresponds to a velocity that is larger than the critical transition velocity ($\mathcal{U}^* > 1$). We observe an expansion of the non-Newtonian domain to the bulk of the pore that is much faster in the case A and P than B and C.

V. DIMENSIONAL ANALYSIS AND TRANSITION THEORY

In this Section, we detail the theoretical derivation of the critical velocity, which leads to the result

$$\langle U_c \rangle_{\mathrm{FL}} \simeq \dot{\gamma}_c \sqrt{k_0}, \tag{2}$$

with k_0 the Newtonian permeability and $\dot{\gamma}_c$ the critical shear rate for non-Newtonian transition. The key to this formulation

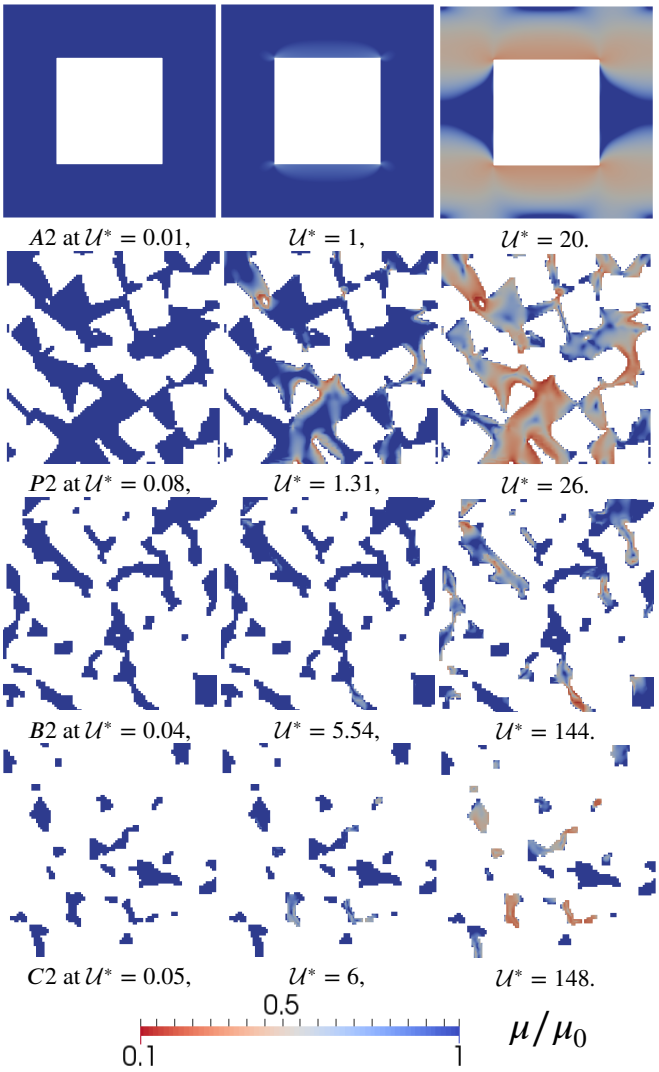

FIG. 2 Dimensionless viscosity fields for media $A2$, $P2$, $B2$ and $C2$ at different flow regimes. Rheology: $n = 0.75$ & $\dot{\gamma}_c = 1s^{-1}$.

is the subdomain Ω_{PT} of the fluid that controls both the transition to the non-Newtonian regime and the viscous dissipation as illustrated in Fig. 3.

The first step of the demonstration is a dimensional analysis of the critical velocity, which leads to

$$\langle U_c \rangle_{\mathrm{FL}} \simeq \dot{\gamma}_c \ell_{\mathrm{eff}}, \tag{3}$$

where ℓ_{eff} is an effective length scale. In this model, the rheology is characterized only by $\dot{\gamma}_c$ while the geometrical properties of the porous medium are embedded in ℓ_{eff}. This formulation is compatible with our computations showing a linear relationship between $\langle U_c \rangle_{\mathrm{FL}}$ and $\dot{\gamma}_c$ and quasi-independence from n (see Fig. 4). Consistent with previous studies ([6–8]) that neglect the influence of the parameter n on the transition, Fig. 4 shows that the critical velocity, $\langle U_c \rangle_{\mathrm{FL}}$, primarily depends on the critical shear rate $\dot{\gamma}_c$. The parameter n, in the range 0.6 to 1.2, which is reasonable for most polymer solu-

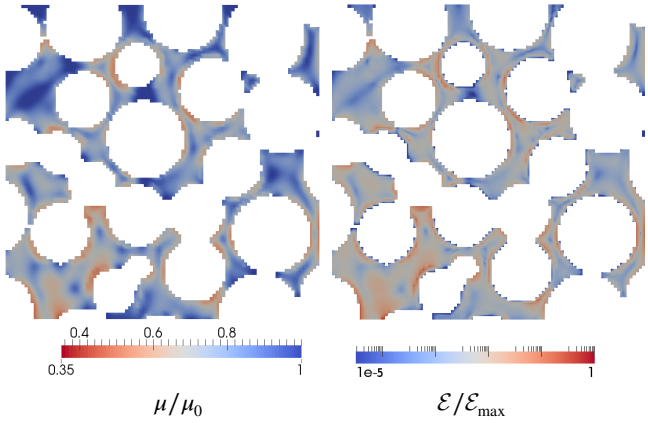

FIG. 3 Comparison of the dimensionless viscosity fields for $P1$ at $\mathcal{U}^* = 1$ (left-hand side) and the local rate of viscous dissipative energy per unit volume normalized by its maximum (right-hand side).

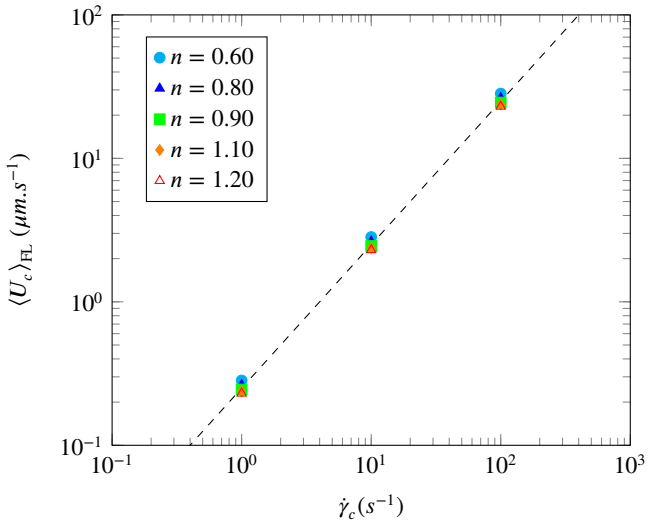

FIG. 4 Critical velocity $\langle U_c \rangle_{\rm FL}$ $(\mu m.s^{-1})$ as a function of $\dot{\gamma}_c$ (s^{-1}) for medium $C1$ and different values of n. Lines are a guide to the eyes.

tions, induces deviations of $\langle U_c \rangle_{\rm FL}$ which are small compared to the impact of $\dot{\gamma}_c$. Given that our dimensional analysis is based on order of magnitudes estimations, we can assume that $\langle U_c \rangle_{\rm FL}$ is independent from n at first order.

To further estimate $\ell_{\rm eff}$, we remark that the transition occurs when the flow in the pore throats becomes non-Newtonian (see Figs. 2 and 3), that is when

$$\langle U \rangle_{\rm PT} = \dot{\gamma}_c \ell_{\rm PT}. \tag{4}$$

Using an acceleration parameter $\beta = \frac{\langle U \rangle_{\rm PT}}{\langle U \rangle_{\rm FL}} > 1$, this can be written as

$$\langle U_c \rangle_{\rm FL} = \dot{\gamma}_c \frac{\ell_{\rm PT}}{\beta}, \tag{5}$$

so that

$$\ell_{\rm eff} = \frac{\ell_{\rm PT}}{\beta}. \tag{6}$$

We then express the permeability for a Newtonian fluid using energetic considerations (see e.g. [9]) as

$$k_0 = \frac{\mu_0 \langle U \rangle^2}{\langle \mathcal{E} \rangle} = \frac{\langle U \rangle^2}{\langle \dot{\gamma}^2 \rangle}, \tag{7}$$

where $\mathcal{E}$ is the local rate of dissipated energy by viscous forces per unit volume. As most of the dissipation occurs in $\Omega_{\rm PT}$ (see Fig. 3), we can further approximate $\langle \dot{\gamma}^2 \rangle \simeq \phi_{\rm PT} \langle \dot{\gamma}^2 \rangle_{\rm PT}$ with $\phi_{\rm PT}$ the volume fraction of $\Omega_{\rm PT}$. A dimensional analysis using a characteristic length $\ell_{\rm PT}$ leads to

$$\langle \dot{\gamma}^2 \rangle \simeq \phi_{\rm PT} \frac{\langle U \rangle^2_{\rm PT}}{\ell^2_{\rm PT}}, \tag{8}$$

and with the acceleration parameter $\beta = \frac{\langle U \rangle_{\rm PT}}{\langle U \rangle_{\rm FL}}$, we have

$$\sqrt{k_0} \simeq \frac{\phi_{\rm FL}}{\sqrt{\phi_{\rm PT}}} \frac{\ell_{\rm PT}}{\beta}. \tag{9}$$

Finally, we define precisely the domain $\Omega_{\rm PT}$ as the domain that is non-Newtonian when the average velocity reaches its critical value $\langle U_c \rangle_{\rm FL}$, so that we can estimate $\sqrt{\phi_{\rm PT}}$ numerically. Results in Table I show that $\frac{\phi_{\rm FL}}{\sqrt{\phi_{\rm PT}}} \simeq 1$ for all the different media, so that $\sqrt{k_0} \simeq \frac{\ell_{\rm PT}}{\beta} < \ell_{\rm PT}$, and finally

$$\ell_{\rm eff} \simeq \sqrt{k_0}. \tag{10}$$

* yohan.davit@imft.fr

[1] A. Jongerius, D. Schoonderbeek, A. Jager, and S. Kowalinski, Geoderma **7**, 177 (1972).
[2] I. Cousin, P. Levitz, and A. Bruand, Eur. J. Soil Sci. **47**, 439 (1996).
[3] M. Ioannidis, M. Kwiecien, and I. Chatzis, Soc. Petrol. Eng. J. **16**, 251 (1996).
[4] O. Rozenbaum and S. R. du Roscoat, Phys. Rev. E **89**, 053304 (2014).
[5] S. S. Datta, H. Chiang, T. Ramakrishnan, and D. A. Weitz, Phys. Rev. Letters **111**, 064501 (2013).
[6] G. Chauveteau, J. Rheol. **26**, 111 (1982).
[7] R. S. Seright, T. Fan, K. Wavrik, R. d. C. Balaban, *et al.*, Soc. Petrol. Eng. J. **16**, 35 (2011).
[8] P. Zitha, G. Chauveteau, and A. Zaitoun, in *SPE International Symposium on Oilfield Chemistry* (1995).
[9] M. Pilotti, S. Succi, and G. Menduni, Europhys. Letters **60**, 72 (2002).